Micro-scale structural and chemical characterisation of deformed rocks with simultaneous in-situ synchrotron X-ray fluorescence and backscatter diffraction mapping

C.E. Schrank [a,*], M.W.M. Jones [b], D.L. Howard [c], A. Berger [d], M. Herwegh [d]

[a] School of Earth and Atmospheric Sciences, Planetary Surface Exploration Group, and Centre for Data Science, Queensland University of Technology (QUT), Brisbane, Australia
[b] School of Chemistry and Physics, Planetary Surface Exploration Group, and Central Analytical Research Facilities, Queensland University of Technology (QUT), Brisbane, QLD, Australia
[c] Australian Nuclear Science and Technology Organisation, Australian Synchrotron, Clayton, VIC, Australia
[d] Institute of Geological Sciences, University of Bern, Bern, Switzerland

ARTICLE INFO

ABSTRACT

In-situ measurements of structural and chemical information on deformed rocks are required to understand microphysical deformation mechanisms, the relative timing of tectono-metamorphic events, and the interplay between deformation, fluid flow, and mineral reactions. Scanning-electron microscopy is commonly used for this purpose, because it can provide compositional information (via energy- or wavelength-dispersive spectroscopy and backscattered electron imaging) and crystallographic orientation data (via electron backscatter diffraction) for large fractions of thin sections down to nanometre resolution. However, elemental and crystal-structural data are usually acquired independently, introducing the need for registration of maps with different information and increasing instrument time. In addition, measuring element concentrations to levels below 1000 ppm increases acquisition times significantly, rendering the mapping of centimetre-scale areas with micrometre-resolution or below time-costly. Here, we introduce an alternative method using coeval synchrotron X-ray fluorescence microscopy (XFM) and X-ray backscatter diffraction mapping (XBDM) for the rapid acquisition of structural and compositional information down to the ppb level on whole rock sections with a spatial resolution down to ~1 μm per pixel. We illustrate the principles of XFM/XBDM mapping on a sample of granitic mylonite. As example for the scientific potential of the new method, it is shown that the Ti distribution in quartz and feldspar can be accurately correlated with physical structure. A discussion of the limitations and opportunities of XFM/XBDM mapping for studying deformed rocks concludes this article.

1. Introduction

Microstructural and microchemical analyses of deformed rocks provide crucial information on some of the most important aspects of faulting, for example, temperature (Law, 2014; Stipp et al., 2002), pressure (Bestmann and Pennacchioni, 2015; Catlos et al., 2018), deformation mechanisms (Passchier and Trouw, 2005), rheological properties and applied strain rate or differential stress (Ebert et al., 2007; Herwegh et al., 2008; Hirth et al., 2001), and fingerprinting of fluid flow and synkinematic mineral reactions (Berger et al., 2017; Ceccato et al., 2022; Tannock et al., 2020). In this context, electron microprobe analysis (EMPA) and scanning-electron microscopy (SEM)

have become the most common non-destructive analytical methods for the microstructural and -chemical characterisation of rock samples. A comprehensive discussion of EMPA and SEM methodology can be found in dedicated textbooks (e.g., Reed, 2005; Schwartz et al., 2009). Briefly, the most important electron-beam methods for microstructural and -chemical characterisation of fault rocks are backscattered electron (BSE) imaging, energy- and wave-length dispersive X-ray spectroscopy (EDS and WDS, respectively), as well as electron backscatter diffraction (EBSD). In BSE imaging, elastically backscattered electrons ejected from a sample depth on the order of 1 μm are measured (Reed, 2005). The backscattering coefficient, i.e., the fraction of incident electrons that are backscattered elastically, is proportional to the atomic number Z.

Therefore, BSE mapping is well suited for phase identification and delineating phases, phase boundaries, and voids in the specimen (Gilgannon et al., 2020; Kanaori et al., 1991) but struggles to visualise the boundaries of grains consisting of the same phase (Herwegh, 2000). EDS/WDS mapping records spectra from characteristic X-rays produced by electron transitions in between bound orbits induced by the electron bombardment of the sample, usually at sample depths <5 μm (Reed, 2005). EDS detectors record X-rays across the entire energy spectrum coevally while WDS detectors are tuned to specific energies (wavelengths) using several suitable crystals. EDS mapping has higher count rates and is considerably faster than WDS but has higher detection limits and lower energy resolution. Therefore, the former is typically used for qualitative elemental mapping and mineral identification, usually in conjunction with BSE maps (Gottlieb et al., 2000; Hrstka et al., 2018), while the latter is used for quantitative microchemical analyses and age dating (Ebert et al., 2007; Raimbourg et al., 2008). Finally, EBSD is an electron-diffraction method employed for the mapping of the crystallographic orientations of grains, residual stress and strain, and phase identification through the analysis of Kikuchi diffraction patterns, probing to a sample depth of ca. 20 nm (Schwartz et al., 2009; Wright et al., 2011). Because the probed sample volume is very close to the surface, great care must be taken during sample preparation to avoid surface damage and topography. Modern SEMs can be equipped with BSE, EDS, and EBSD detectors and thus serve as powerful tools for high-resolution, spatially resolved, chemical, and structural mapping of rocks in geological laboratories.

In this contribution, we introduce a complementary scanning X-ray microscopy (SXM) methodology for heterogeneous rock specimens using synchrotron radiation, that records elemental and structural information rapidly over larger areas with micro-sale resolution. SXM delivers many different types of information. In geological applications, X-ray fluorescence microscopy (XFM) is probably the most popular SXM method because it produces high-resolution (typically down to ~1 μm/pixel for large geological samples) elemental concentration maps rapidly for complete rock sections by measuring emitted fluorescent X-rays with a detector placed upstream of the sample, either in line with the X-ray beam (backscatter geometry), or orthogonal to the X-ray beam with the sample placed at 45° to both the X-ray beam and the detector (Howard et al., 2020). XFM beamlines at synchrotron light sources typically employ multi-detector arrays (Howard et al., 2020; Ryan et al., 2010), which, together with the extremely bright monochromatic synchrotron X-rays, allow the simultaneous high-resolution mapping of >20 chemical elements heavier than Mg with concentrations down to the ppb level across entire thin sections in a matter of hours (Akker et al., 2021; Barnes et al., 2020), surpassing the detection limits, speed, and number of elements that can be recorded with EDS and WDS detectors (von der Heyden, 2020). Because of this capability, XFM was recently hailed as frontier technology for the study of ore systems that should become standard for mineral exploration and the design of metallurgical-beneficiation as well as environmental-mitigation strategies (Stromberg et al., 2019).

Structural information is not obtained directly in an XFM measurement and can therefore only be inferred from the elemental as well as elastic and inelastic scatter maps. The scatter maps provide information analogous to BSE maps discussed previously. To overcome this limitation, XFM is increasingly acquired coevally with complementary methods. The coeval application of multiple methods provides fundamental advantages: immediate error-free registration between elemental and structural maps is possible; and the sample is measured in the same state during both imaging methods, which is particularly useful for dynamic in-situ studies (van Riessen et al., 2017). Because fluorescence detectors typically occupy the space upstream of the sample to collect emitted X-rays (either in backscatter or orthogonal geometry), additional detectors for the acquisition of structural information coevally with XFM need to be placed downstream of the sample, thus collecting transmitted X-rays. Compatible techniques include Laue

microdiffraction (Hamilton et al., 2018), scanning X-ray diffraction (Egglseder et al., 2019; Gueriau et al., 2020), scanning small-angle X-ray scattering (Lapkin et al., 2022), and X-ray ptychography (Jones et al., 2022; Pfeiffer, 2018; Schrank et al., 2021). However, transmission X-ray techniques integrate the entire thickness of the sample and its support (e.g., a microscopy slide) at each measurement point. Thus, samples must be kept thin (tens of micrometres) and ideally free-standing to avoid overprinting of structures caused by grains smaller than the sample thickness or a sample holder contributing background scatter. The preparation of free-standing rock slabs with micrometre thickness is achievable for small sub-millimetre samples. However, as soon as the sample width increases to the centimetre scale, preparing such thin, free-standing sections becomes increasingly problematic. Obtaining coeval structural information from backscattered X-rays from the upper tens of micrometres of the sample (depending on the incident beam energy) eliminates these sample preparation limitations, allowing geological thin sections (even exceeding thicknesses of 30 μm) to be easily mounted on a fused-quartz microscope slide, simplifying sample handling, and permitting traditional petrographic imaging before and after X-ray analysis.

Recently, coeval scanning X-ray backscatter diffraction mapping (XBDM) and XFM were demonstrated by separating elastic diffraction peaks from fluorescence data recorded by the 384-element Maia detector in the backscatter geometry (Kirkwood et al., 2018), overcoming the need for strict thickness requirements. Moreover, coeval XFM and XBDM has been applied using the two-detector PIXL X-Ray Fluorescence (XRF) instrument on the Perseverance rover to identify individual contiguous grains with the same crystallographic orientation in whole rock samples in situ on the surface of Mars (Liu et al., 2022; Tice et al., 2022). Here, we present the application of synchrotron-based coeval XFM and XBDM to a section of a granitic mylonite (Fig. 1) at 2 μm resolution, measuring >20 trace elements together with grain structural information extracted from the elastic diffraction signal (Fig. 2), and discuss its potential for the characterisation of deformed rocks.

2. Material and methods

2.1. Geological background of the sample

We chose a granite-derived mylonite sample for this study because it contains deformation microstructures characteristic of typical crustal rocks sheared under greenschist-facies conditions that can be easily recognised in transmitted-light micrographs, namely dynamically recrystallised quartz ribbons, feldspars with both brittle and crystal-plastic deformation structures, and syntectonic and inherited micas and epidote (Fig. 1). The sample derives from an Alpine granitoid shear zone of the of the Aar Massif (Central Alps, Switzerland). The Aar Massif is one of the External Crystalline Massifs (ECM) of the Alps, which represent a late stage of the Alpine collision manifested by extruded European continental crust (Herwegh et al., 2017). The ECM in general, and the Aar-massif in particular, are dissected by numerous shear zones with reverse shear sense (Wehrens et al., 2017; Wehrens et al., 2016). The sample investigated in this study comes from the post-Variscan Central Aare granite of the Aar-massif (298 +/− 2 Ma (Schaltegger and Corfu, 1992)), which was intensively subjected to buoyancy-driven vertical tectonics during late Alpine convergence (~22 Ma (Herwegh et al., 2017; Herwegh et al., 2020)). This stage is manifested by substantial vertical rock uplift exhuming maximal upper greenschist metamorphic conditions (6 ± 1 kbar/ 450 ± 30 °C (Challandes et al., 2008; Goncalves et al., 2012)), followed by nearly isothermal decompression (Herwegh et al., 2020). In terms of general background low-strain deformation, granitoid host rocks show flattening fabrics (Choukroune and Gapais, 1983; Wehrens et al., 2017), characterized by parallelization of biotite and feldspars (Figs. 1). The latter show embrittlement in combination with alteration processes (see also Section 3.1), resulting in neocrystallization of fine-grained sericite, albite, K-
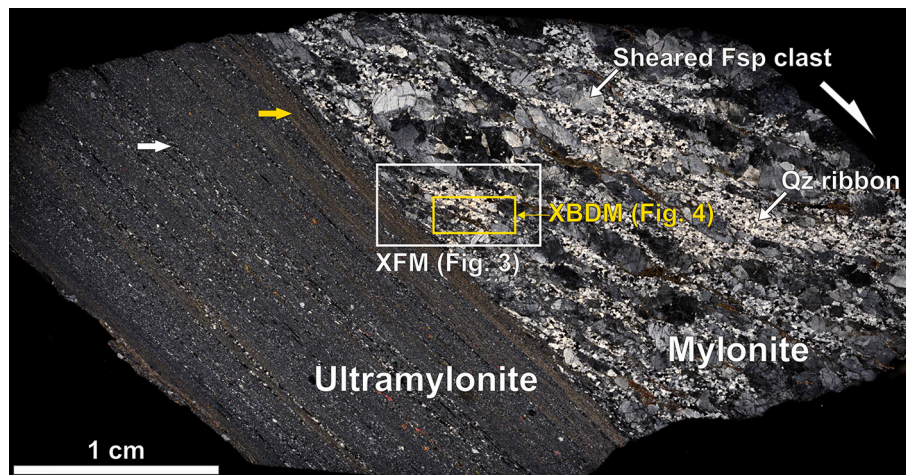
Fig. 1. Transmitted-light micrograph of the studied mylonite sample (crossed polarisers). The white rectangle marks the XFM overview map (Fig. 3), which contains the contact between mylonite and ultramylonite. The yellow rectangle indicates the region mapped with XBDM (see also Fig. 4). Dextral shear sense is readily asserted by the drag of quartz ribbons (see annotated example) and discontinuous cleavage domains into the ultramylonitic section as well as various shear sense indicators associated with feldspar clasts (see annotation). Tectosilicate- (white arrow) and epidote−/mica-rich bands (yellow arrow) alternate in the ultramylonite (see also Fig. 3e). (For interpretation of the references to colour in this figure legend, the reader is referred to the web version of this article.)
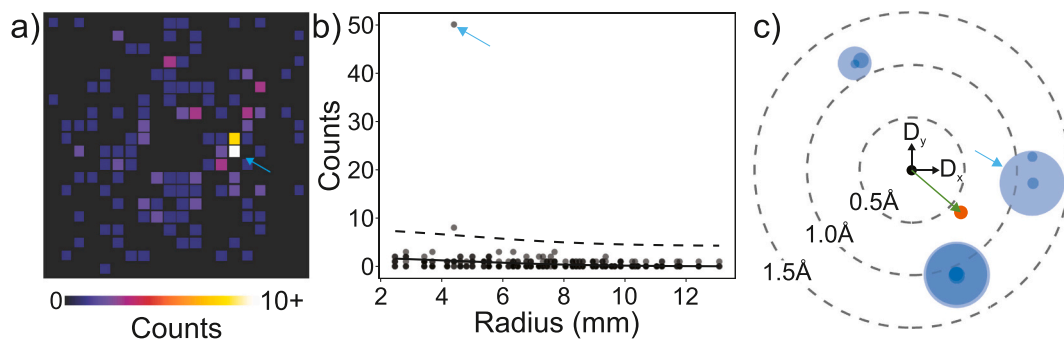

Fig. 2. XBDM data processing scheme for a fixed scan position (i.e., image pixel). a) Elastic scatter in the Maia detector at a single energy and scan position (image pixel). b) Plot of photon counts per Maia detector element over the radius from the beam axis for data shown in a). A Gaussian fit to the elastic scatter (solid line) is used to determine a threshold (dashed line, Eq. (1)) above which a scattering event is considered as diffraction. c) Visualisation of the combined diffractions collected from the multi-energy scan represented in d-space. The blue circles represent a detected diffraction peak, and their size corresponds to peak intensity, with three clear diffraction spots in this example. The black dot at the centre represents the beam axis, the orange dot is the calculated centre of mass (CoM), and the green arrow the position vector of the CoM. The blue arrows in all panels mark the same diffraction peak. This process is repeated for all scan positions to build up the XBDM map. (For interpretation of the references to colour in this figure legend, the reader is referred to the web version of this article.)

feldspar, and epidote. Former interstitial quartz has been deformed completely in a ductile manner, forming elongated anastomozing bands enclosing the rigid feldspar clasts (Fig. 1) and giving the Central Aare granite outside the shear zones a gneissic appearance. Quartz shows grain size reduction to about 100 μm by subgrain rotation recrystallization forming crystallographic preferred orientations (Bambauer et al., 2009; Wehrens et al., 2016).

The most pronounced microstructural changes occur in subvertical shear zones with reverse-fault kinematics and widths from a few centimetres to metres. In these shear zones, the grain sizes of the former granitoid reduces dramatically, resulting in polymineralic bands with grain sizes ≤10 μm (Fig. 1; Wehrens et al. (2016)). The related mineral assemblage consists of quartz, albite, K-feldspar, biotite, white mica, and epidote in the gneissic and ultramylonitic parts (see Section 3.1, Fig. 1). These ultramylonites deformed by viscous granular flow (Berger et al., 2017; Wehrens et al., 2017; Wehrens et al., 2016) and consist of mineralogically distinct bands a few tens of micrometres wide, owing to high strain of quartzo-feldspathic or epidote-rich protolith domains (Fig. 1). These shear zones accommodated high-strain non-coaxial deformation, pervasively dissecting the gneissic Central Aare granite host. After the reverse-faulting stage, exhumation of the Aar massif took

place by thrust-related vertical tectonics (< 12 Ma, Herwegh et al. (2020)), and a recent stage of nearly subvertical rock uplift at 1 mm/a. These later deformation stages did not affect the sample investigated in this study.

2.2. Sample preparation and light microscopy

A hand specimen featuring the transition from mylonite to ultramylonite was cut perpendicular to the foliation and parallel to the stretching lineation. A polished section of ca. 30 μm thickness was prepared on a high-purity quartz slide with dimensions 50.8 × 25.4 mm without cover slip for XFM/XBDM analysis (Fig. 1). Thin-section transmitted light micrographs in plane- and cross-polarised light were acquired with the Olympus VS200 Slide Scanner (Acevedo Zamora and Kamber, 2023) at ten-times magnification for the entire slide (Fig. 1) and forty-times magnification for the regions studied with XFM (see Section 3.1).

2.3. XFM

The sample was presented to the XFM beamline at the Australian

Synchrotron (Howard et al., 2020) for analysis using standard sample mounts. An overview map of 8 mm × 4 mm (Fig. 1) was scanned continuously at a velocity of 2 mm s^{-1} with a sampling interval of 2 μm, in both the horizontal and vertical direction, through an 18.5 keV X-ray beam focused to a ∼ 2 μm spot at the sample, using a Kirkpatrick-Baez mirror pair. The total scan time amounted to ∼135 min. Excited X-ray fluorescence was collected in event mode using a Maia (Rev D) detector system (Ryan et al., 2018; Siddons et al., 2014) positioned in its typical backscatter geometry. The Maia detector consists of 384 energy-dispersive detector elements, each measuring ∼1 × 1 mm, arranged in a 20 × 20 grid (Siddons et al., 2014). The 16 central elements are removed to allow the beam to pass through. The detector array subtends a large solid angle of 1.3 sr. Spectra were deconvoluted using the Dynamic Analysis (Ryan and Jamieson, 1993) method implemented in GeoPIXE (Ryan et al., 2005) and quantified using known metallic foils, producing quantitative images of elements from sulphur to zirconium.

2.4. XBDM

A smaller area of approximately 4 mm × 1.8 mm (Fig. 1) was selected from the overview map and scanned similarly as described in Section 2.3. However, to collect elastic scatter, scan energy was varied over 24 energies, from 5205 eV to 5895 eV, in increments of 30 eV. Each scan took ca. 31 min. This strategy was employed for the following reasons. First, the lower energy provides an increased absorption cross-section for light elements such as Ti, yielding a higher signal-to-noise fluorescence signal than at higher energy and thus improved trace-element maps. Second, the low energy increased the spacing of the diffraction peaks at high diffraction angles (126° < 2θ < 169°), which minimises the chance of recording multiple Bragg peaks within the same detector element of the Maia detector in the backscatter geometry. Third, the lower scanning energy reduced X-ray penetration depth and thus also the background elastic-scatter contribution from the quartz glass slide. Fourth, varying the energy compensates for the limitation that neither the detector nor the sample can be rotated relative to the beam. At a single fixed energy, sample, and detector configuration, some grains might not satisfy the Bragg condition geometrically and thus do not produce observable elastic scattering.

Elastically scattered photons were extracted from the Maia event stream using an energy window of 260 eV (the approximate energy resolution of the detector) centred around the incident beam energy (Fig. 2a). We define the sum of the unprocessed elastic scatter intensities at a single energy and given scan position (i.e., each image pixel) as the "scattering intensity" in the following. This scattering intensity entails two phenomena: the uniform scattering background, proportional to Z, and the sum of the Bragg-reflected photons, incorporating the intensity and number of peaks. The number of Bragg reflections in a scattering volume is roughly proportional to the size of the unit cell and depends on crystal orientation (see also Section 4.1). Therefore, the scattering intensity conveniently portrays differences in bulk elemental composition, unit cell size, and crystal orientation as a single scalar, permitting rapid visualisation of mineral grains without the need for additional data processing (see Section 3.2). To separate the Bragg reflections from the background scatter (Fig. 2b), a Gaussian curve, $G(r)$, is fitted to the number of recorded photons in each detector element as a function of the respective radius of each detector element from the beam axis, r, which is used to generate a threshold, $T(r)$, defined as:

$$T(r) = A\sqrt{G(r) + n} \tag{1}$$

where A and n are constants as defined in Orenstein et al. (2023). In this case, we use a conservative threshold with $A = 3$ and $n = 2$ to limit detection of false peaks.

The diffraction events recorded across the energy scans form a discrete energy-dispersive XRD dataset. To combine the energy scans into a single XBDM map, the 2θ angle for each diffraction event was converted to d-spacing via Bragg's law, preserving angular information, before being combined in d-space (Fig. 2c). To represent the dataset in a 2D map, the centre of mass (CoM) was calculated for all elastic diffractions at a given scan position (image pixel) in d-space, using the position coordinates D_x and D_y of each Bragg reflection weighted by the photon counts above threshold T (Fig. 2c). The position vectors for the CoM (green arrow in Fig. 2c) are used for visualisation (Figs. 6, 7).

2.5. EBSD

For comparison with the elastic-scattering maps, we imaged a square region with an edge length of 250 μm featuring quartz grains only with EBSD. A JEOL 7001F Scanning Electron Microscope with Oxford EBSD system was employed. EBSD mapping was conducted with 30 kV acceleration voltage at a specimen tilt of 70° and acquisition rate of 13.33 Hz for 1 × 1 μm steps with 4 × 4 binning. Acquisition time amounted to ca. 78 min. Quartz was indexed via the instrument's software database HKL. 27.53% of the 250^2 interrogated pixels delivered valid solutions with a mean angular deviation of 0.99 (standard deviation: 0.24) and mean band contrast of 64.24 (standard deviation of 10.87). The indexed dataset was exported via Aztec 3.3 and further processed and visualised with MTEX 5.9.0 (Bachmann et al., 2010).

3. Results

3.1. Microstructural sample description

Polarisation micrographs reveal that the foliation in the mylonitic part of the sample consists of microlithons, dominantly composed of quartz ribbons, bands of recrystallised feldspars and quartz, and clasts of K-feldspar as well as albite, and discontinuous cleavage domains, mainly containing mica and epidote (Figs. 1, 3a, b). Quartz ribbons are made of polygonal grains with straight grain boundaries with many triple-point boundary angles close to 120°, aspect ratios generally <2, and median grain diameter of 66 μm. Optical interference colours within individual quartz grains appear largely homogeneous, suggesting low dislocation density within grains. In concert, this microstructure suggests that magmatic quartz grains of the granitic protolith underwent a grain-size reduction process via dynamic recrystallisation followed by minor annealing.

Feldspar clasts in the mylonitic section show neocrystallisation and brittle fracturing, including domino- and shear-band-type fragmentation, accompanied by internal crystal-plastic deformation structures such as kinked twins, undulose extinction, and subgrains (Fig. 3b). Fractures are commonly decorated with epidote, white mica and biotite, K-feldspar, and occasionally secondary quartz. Recrystallised albite grains with typical lengths between 10 and 50 μm sometimes form thin (∼100 μm thick) bands or incipient mantle structures around fractured magmatic feldspar clasts (Fig. 3b).

The ultramylonitic portion of the thin section (Fig. 3e) is made of parallel, straight (unless when wrapping around a feldspar clast at the interface with the mylonite), quartzo-feldspathic and mica−/epidote-rich layers with thicknesses between 10 and 450 μm. All elongated grains show a strong shape-preferred orientation parallel to the compositional foliation. Micas have mean lengths of ca. 27 μm with average aspect ratio of 4.5 while epidote and recrystallised tectosilicate grains have a mean long-axis length of ca. 15 μm with an average aspect ratio of ∼2.

3.2. Scattering intensity

Let us compare a map of the scattering intensity recorded at a fixed single energy with a transmitted-light micrograph obtained under cross-polarised light (XPL) (Fig. 4a, b). The scattering intensity is highly sensitive to the crystal-lattice orientation and mineral species. For example, individual recrystallised grains within quartz ribbons can be
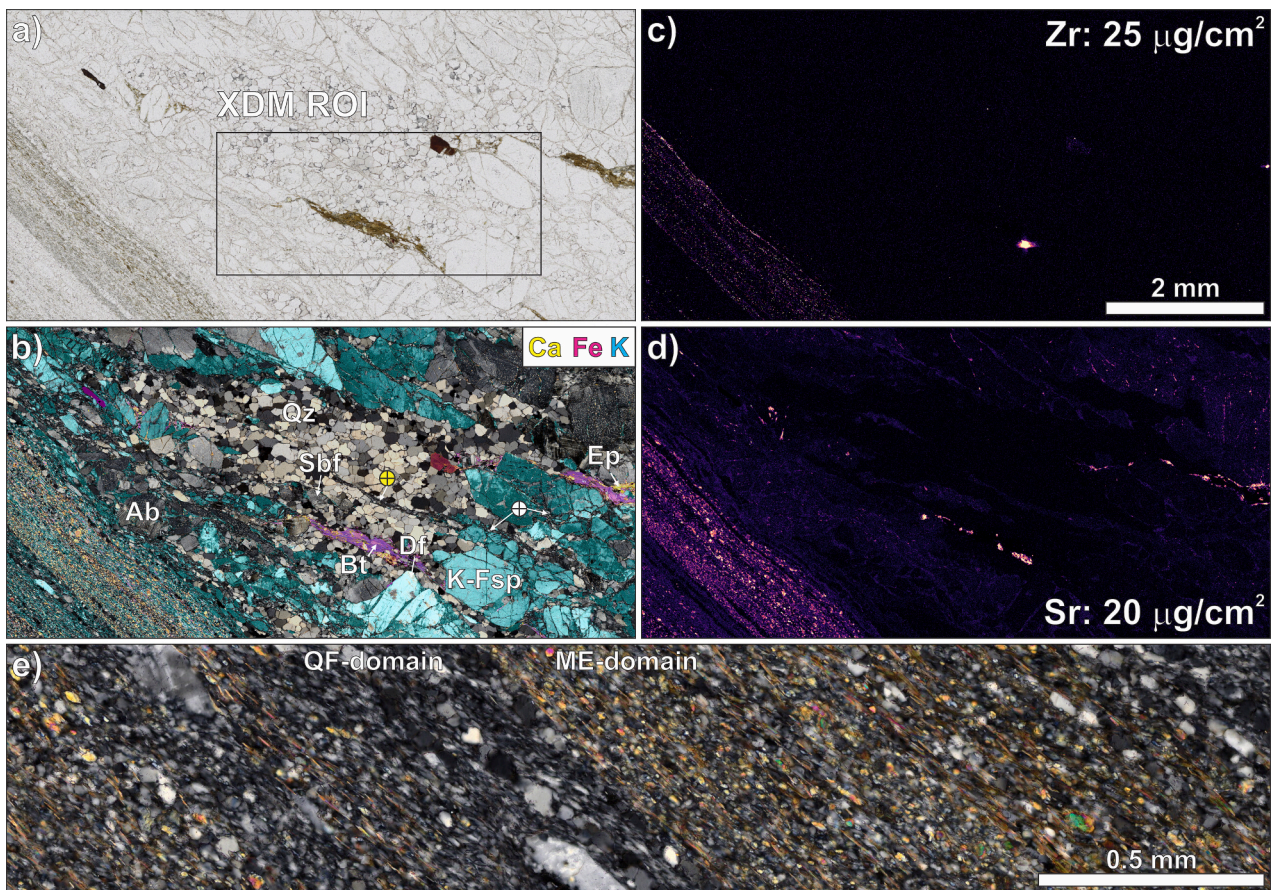
Fig. 3. Micrographs (a, b, e) and two XFM maps of sample revealing the transition from mylonite to ultramylonite. (a) Micrograph observed in plane-polarised light. The black rectangle marks the region of interest (ROI) analysed with XBDM, shown in Figs. 4 and 5 and elsewhere. (b) Micrograph with cross-polarised light overlain with XFM maps for the elements Ca (yellow), Fe (magenta), and K (cyan), facilitating recognition of feldspars, epidote, and biotite. Ab: albite, Bt: biotite, Ep: epidote, K-Fsp: K-feldspar, Qz: quartz. Sbf: shear-band-type fragmentation, Df: domino-type fragmentation, white crossed circle: recrystallised albite encasing broken K-feldspar clasts, yellow crossed circle: band of recrystallised albite. (c) The Zr map of the sample reveals that micro-scale Zr-rich grains, probably zircons, are enriched most at the interface between mylonite and ultramylonite, suggesting significant volume loss through dissolution during ultramylonite formation. (d) The Sr map shows that this trace element is largely hosted in epidote, which is one of the main constituents of the ultramylonite. The scale bar for panels a) to d) is shown in c). (e) Magnified view of the ultramylonitic region, highlighting a quartzo-feldspathic layer (QF domain) and a mica- and epidote-rich layer (ME domain). (For interpretation of the references to colour in this figure legend, the reader is referred to the web version of this article.)

recognised in the unprocessed scattering maps (Fig. 4a, c). Fractures and crystal-plastically deformed regions within feldspar are reflected by strong local variations in scattering intensity (Fig. 4a, b, d). Histograms for the scattering intensity of quartz, mica, K-feldspar, and albite grains overlap but exhibit distinct modes (Fig. 4f), explaining why regions of the scattering-intensity map occupied by quartz appear darker on average than those occupied by feldspar (compare Fig. 4b and e).

3.3. Total number of elastic reflections NR

Integrating the entire energy-dispersive scattering dataset, maps of the total number of elastic Bragg reflections (NR) per image pixel were produced, counting each reflection with unique coordinates D_x and D_y relative to the Maia detector once, regardless of energy. Only 0.13% of all mapped pixels did not return any elastic reflections. This excellent coverage demonstrates that the employed energy-dispersive approach to mapping elastic scattering compensates for the lacking tilt capability of the sample and detector. The NR map (Fig. 5a) shows that each mineral phase presents a characteristic range of reflection counts (Fig. 5b, Supplementary Table 1). The modes of the NR distribution for quartz, mica, albite, and K-feldspar are 7, 22, 48, and 58, respectively. This observation suggests that it will be possible to index the Bragg reflections and determine the lattice orientation for most interrogated pixels of the main

mineral phases with the look-up table method used by Kirkwood and collaborators (Kirkwood et al., 2018). These authors demonstrated that, in practice, at least four linearly independent reflections are required for indexing and orientation analysis. We find that in quartz >94% of all interrogated pixels recorded 4 or more elastic reflections. This proportion is >99.9% for all remaining main phases (Supplementary Table 1). In addition, NR displays a marked increase or gradient at, or adjacent to, interfaces between grain, subgrains, cracks, and regions with different lattice orientations within grains (Fig. 5c–f) and is thus very well suited to mapping these features.

3.4. Centre of Mass (CoM) of elastic reflections

The XPL micrograph and a scalar map of the CoM vector field are compared in Fig. 6. Individual grains, subgrains, twins, and intra-granular regions with crystal-plastic deformation are readily recognised in both images. In addition, the CoM vector-length distribution is phase-specific (Fig. 6b). Quartz grains appear in the most saturated colours because, on average, their CoM vectors are longer (mode = 0.33 Å, median = 0.42 Å, mean = 0.45 Å) than those of the other main minerals (mica: mode = 0.27 Å, median = 0.32 Å, mean = 0.34 Å; albite: mode = 0.19 Å, median = 0.25 Å, mean = 0.26 Å; K-spar: mode = 0.18 Å, median = 0.21 Å, mean = 0.22 Å).
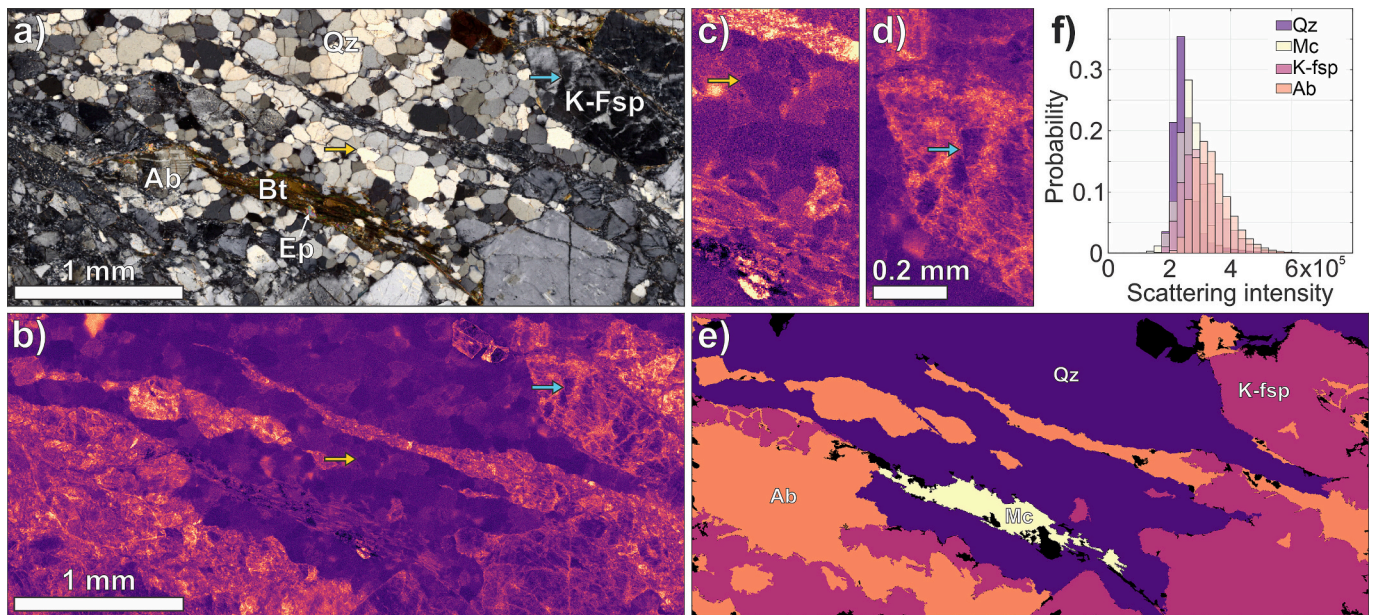
Fig. 4. Comparison of XPL micrograph and scattering-intensity map. a) Sample micrograph under XPL. b) Map of the scattering intensity recorded at 5895 eV. c) Contrast-enhanced magnified view of a quartz-rich region. The yellow arrow acts as location reference for panels a) and b). d) Magnified view of a feldspar clast with a blue arrow as location reference to panels a) and b). e) Quartz (Qz), K-feldspar (K-fsp), albite (Ab), and mica (Mc) segmented via XFM maps of Ca, K, and Si. This segmentation is used for the determination of all phase-specific statistics reported in this article. f) Associated histograms of scattering intensity extracted from the map panel b). (For interpretation of the references to colour in this figure legend, the reader is referred to the web version of this article.)
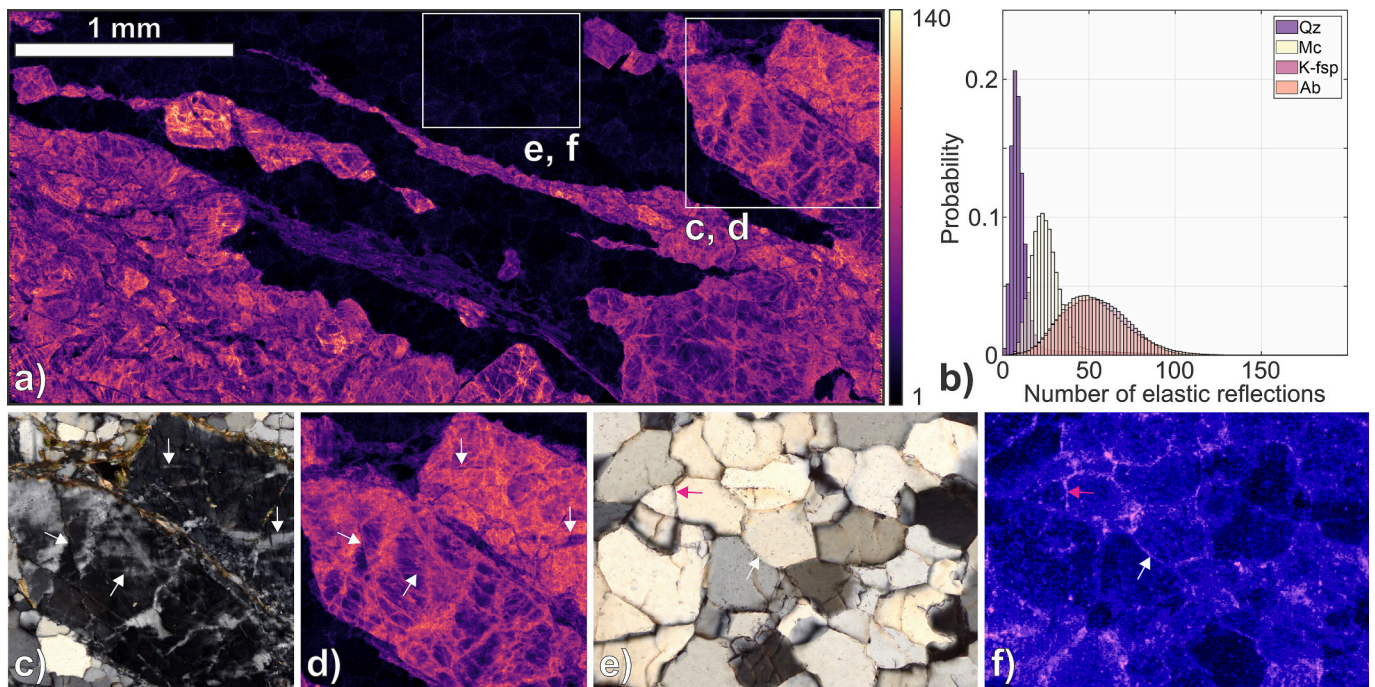

Fig. 5. a) Map of the total number of Bragg reflections NR recorded in each pixel. b) Histograms of NR for the four main mineral phases quartz, mica, K-feldspar, and albite. A magnified view of the fractured K-feldspar clast in the upper-right corner of the NR map is shown in transmitted light (crossed polarisers) in panel c), accompanied by the related NR map in d). Panels e) and f) display equivalent magnified views for a quartz ribbon. Arrows in panels c) to f) mark corresponding points in paired maps on c), d) interfaces of cracks and crystal-plastically deformed regions, and e), f) grain boundaries. The colour scale in f) differs from that in a) because it is adjusted for the lower NR values in the quartz ribbon.

Superposing the CoM-position vectors onto XPL micrographs high-lights how sensitive CoM vectors are to changes in crystal-lattice orientation and composition (Fig. 7a, d). Even the most subtle changes of the interference colours in XPL are reflected in changes of the CoM-position vector field, enabling the recognition of intragranular crystal-plastically deformed regions (Fig. 7a). Inspecting the CoM vector fields together with collocated XFM maps reveals the power of combined XFM/XBDM mapping. For example, the method reveals that the trace elements Ti (with modal concentration < 5 ppm) and Ca (with modal concentration of 51 ppm) are mobilised by crystal-plastic deformation
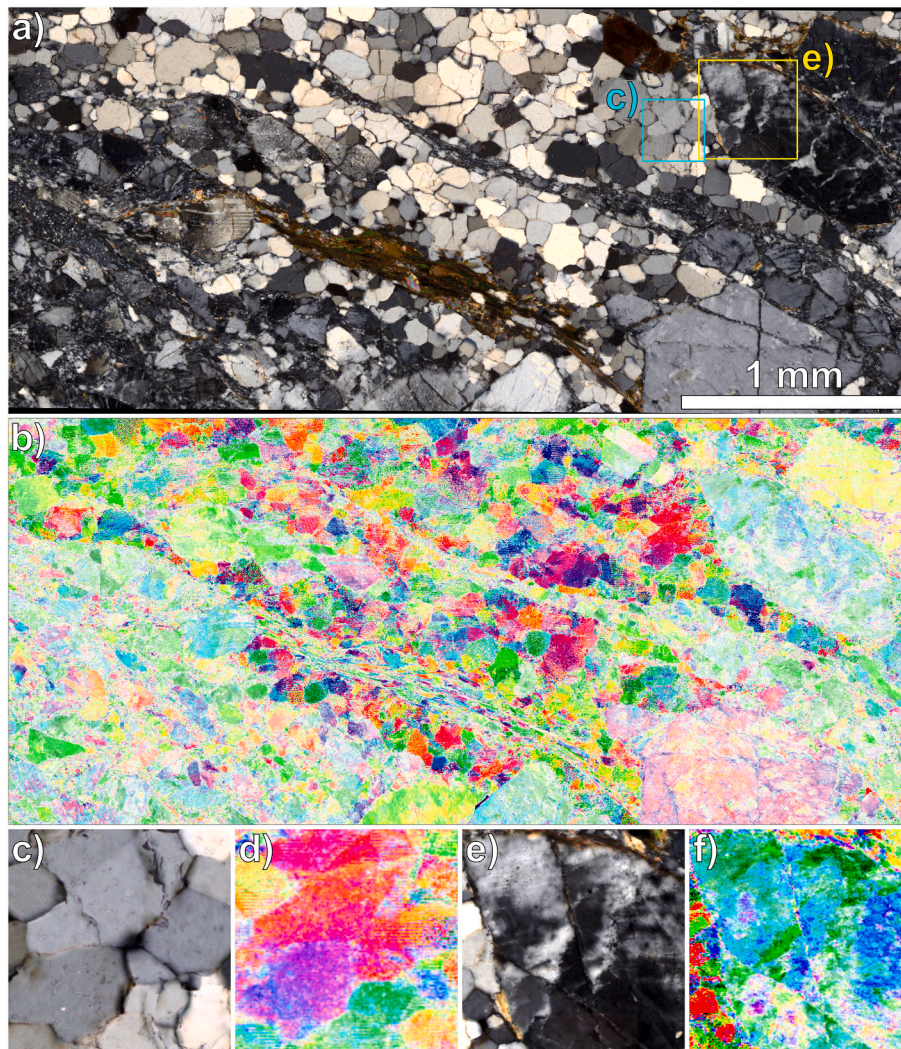
Fig. 6. a) XPL micrograph of the region of interest. The coloured rectangles mark the positions of the magnified views in panels c) and e). (b) Corresponding scalar visualisation of the 2D vector field for the CoM-position vectors (Fig. 2c) using the script of Howe (2023). Pixel hue indicates vector direction while pixel saturation scales with vector magnitude (see also Fig. 7). Maximum saturation is capped at the 95-percentile of the vector-length distribution to enhance contrast. Individual grains are easily recognised as regions with relatively constant colour. Scale is the same as in a). Lower row: Magnified views of the XPL micrograph (a) and the associated CoM map (b) for c), d) a quartz ribbon, and e), f) a deformed magmatic K-feldspar clast. The CoM map in f) is contrast-enhanced relative to panel b) to better show CoM variations within the K-feldspar clast.

and fracturing within a magmatic K-feldspar clast (Fig. 7a-c). Similarly, it becomes possible to differentiate between Ti- and Fe-bearing phases in quartz ribbons buried within the thin section, that formed as intra-granular inclusions, and later phases decorating quartz grain boundaries, potentially grown during the dynamic recrystallisation of quartz (Fig. 7d–f, Wehrens et al. (2016)). The trace element Ti is commonly used as thermometer for quartz formation (Wark and Watson, 2006) and, more recently, that of K-feldspar (Zhang et al., 2022). To constrain the applicability and correctly interpret such thermometers in natural rocks requires the careful grain-scale study of Ti mobilisation by later fluids and deformation (e.g., Bestmann et al., 2021). XFM/XBDM mapping constitutes an excellent tool for this purpose.

4. Discussion

Our results (Section 3) show that coeval XFM/XBDM provides a multitude of co-registered, micro-scale trace-element and scattering information that can be used to identify grain boundaries, sub-grain boundaries, cracks, and zones of crystal-plastic deformation (Figs. 4–6). This information allows researchers to identify the pathways

for fluid-assisted and solid-state mass transfer and map patterns of crystal growth, neocrystallisation, dynamic recrystallisation, and microfracturing (Fig. 7) over millimetre- to centimetre-length scales in relatively short time frames. A discussion of the various XBDM maps, their comparison to EBSD data, optimisation of scanning protocols, and other experimental challenges and opportunities follows.

4.1. Scattering-intensity and NR maps

Our elastic-scattering maps demonstrate that the scattering intensity (Fig. 4) and total number of recorded elastic reflections NR (Fig. 5) are mineral-specific, with quartz giving the lowest numbers and feldspar the highest. This observation is explained by the phase-specific differences in composition and lattice structure. Aside from instrument- and specimen-specific parameters, the position and number of elastic reflections mainly depend on the crystal system (see, for example, eqs. 8.2 to 8.7 in Pecharsky and Zavalij (2009)) while the intensity of elastic reflections is largely controlled by the scattering angle and the structure factor, which depends on the spatial distribution of atoms and their types (Chapter 9 in Pecharsky and Zavalij (2009) elaborates on the
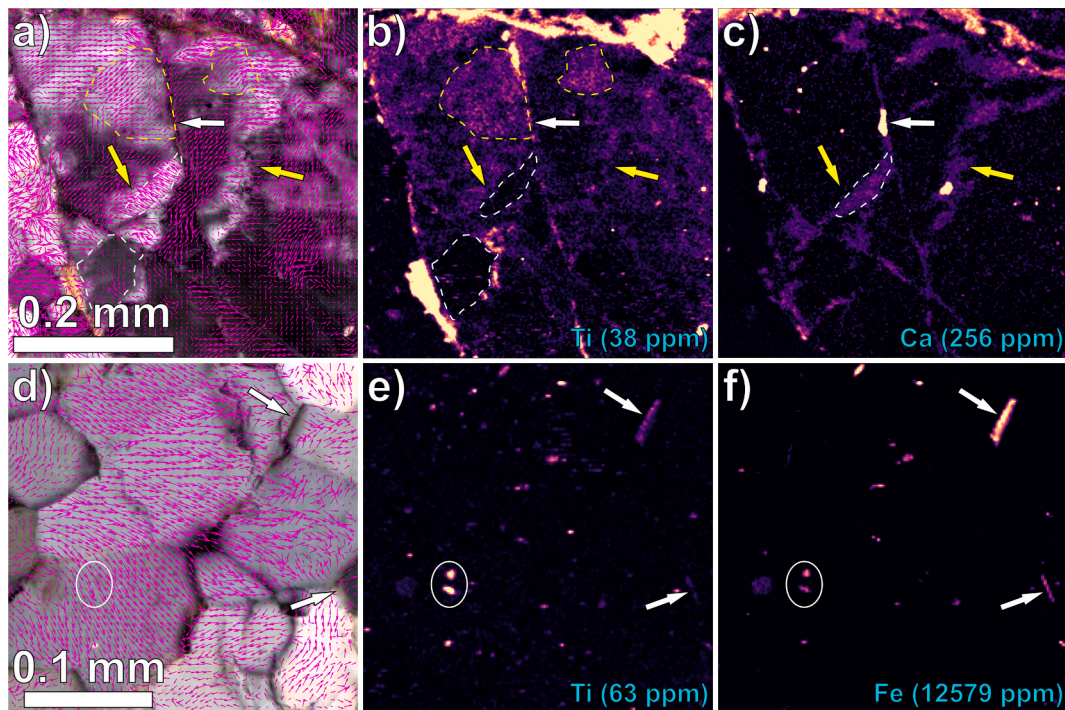
Fig. 7. Additional maps for the magnified regions displayed in Fig. 6c–f. (a) Magnified view of a K-feldspar clast in XPL with superposed CoM vectors. Only ca. 10% of the available vectors are shown for clarity. Changes in the vector field reflect even the most subtle interference-colour changes in the underlying micrograph, caused by intragranular crystal-plastic deformation (yellow arrows) and fracturing (white arrow). The dashed yellow and white polygons mark zones with enrichment and depletion in Ti, respectively, as seen in panel b). These regions internally display similar optical interference colours and CoM-vector orientations, marking subgrains. b) Ti map for the region shown in a). The maximum value of the colour scale is given in the lower-right corner, as in all other elemental maps in this figure. The mode of the Ti distribution within the feldspar clast excluding the fracture is 3.5 ppm. Zones of Ti enrichment and depletion are controlled by intracrystalline structure (dashed polygons). c) Ca map for the region shown in a). The modal concentration of the Ca-enriched zones, such as that marked by the white dashed line, is 51 ppm. d) Magnified view of a quartz ribbon with CoM vectors, also at ca. 10% data density. Individual grains and internal crystal-plastic deformation can be discerned clearly from the vector field. The white arrows mark quartz grain boundaries decorated by platy minerals enriched in Ti and Fe that can only be detected in the associated XFM maps in e) and f) because they are not located at the surface of the thin section. The white oval marks ellipsoidal intragranular Ti- and Fe-enriched phases barely visible in transmitted light. (For interpretation of the references to colour in this figure legend, the reader is referred to the web version of this article.)

structure factor in detail). Trigonal quartz produces the smallest number of Bragg reflections in reciprocal space while the low-symmetry feldspars (triclinic, monoclinic) produce the most, as readily illustrated by their conventional powder-diffraction patterns (Supplementary Fig. 1). Thus, for a given detector configuration and grain orientation, there is a higher probability to detect elastic reflections for feldspar than for quartz with XBDM. This notion is supported empirically by the positive correlation between the number of powder-diffraction peaks (counted to $2\theta = 100°$) and the scattering intensity as well as NR (Supplementary Fig. 2).

Moreover, NR often displays a marked increase at interfaces such as grain boundaries, subgrain boundaries, and cracks (Figs. 5, 7, 8). Nano-

and micro-scale secondary mineral phases decorating these interfaces contribute to this effect, as evidenced by our XFM maps (Figs. 7, 8) and shown by previous microanalytical studies of deformed metamorphic rocks (Herwegh and Kunze, 2002; Kruhl et al., 2013). Grain-boundary dislocations and ledges (Hirth and Balluffi, 1973) can also produce elastic diffractions, provided that they are common enough and spatially periodic (Balluffi et al., 1972). Finally, reflections from multiple grains can be recorded at grain boundaries when adjacent grains overlap within the sample interrogation volume, leading to multi-lattice diffractions and thus increased NR count (Kirkwood et al., 2018). Reducing the integrated volume through a smaller probe or reduced sampling depth would decrease this effect. The example in Fig. 8 shows these
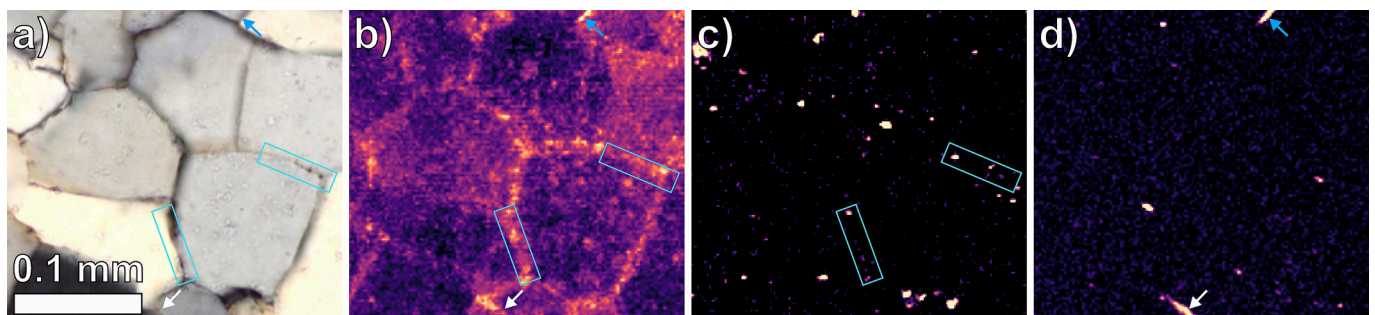

Fig. 8. a) XPL micrograph of a quartz ribbon with corresponding XFM/XBDM maps of b) NR, c) Ca, and d) Fe. Examples of grain boundaries decorated by micron-sized Ca- and Fe-rich phases are marked with rectangles and arrows, respectively.

different effects on the NR map. Quartz grain boundaries are highlighted in the NR map, with and without small secondary minerals detected by element mapping (e.g., Ca, Fe).

4.2. Qualitative comparison of CoM and EBSD maps

A comparison of an EBSD map of a quartz ribbon with the associated CoM map is presented in Fig. 9. Valid EBSD solutions were obtained for <28% of the interrogated pixels while >99% of pixels returned Bragg reflections with XBDM. The reason for the low success rate of EBSD is that the sample surface was not polished to the standard required for optimal EBSD mapping (Fig. 9a). EBSD probes to a sample depth of up to tens of nanometres and is highly sensitive to surface topography (Schwartz et al., 2009; Wright et al., 2011). The micro-scale surface damage induced by standard polishing causes the >70% zero solutions. In contrast, X-ray techniques such as XFM/XBDM are not sensitive to nano- and micro-scale surface damage. Qualitatively, the CoM vector field captures grain and subgrain boundaries identified by EBSD misorientation analysis very well, including those recognised in the XPL micrograph (Fig. 9b–e). To map these boundaries from the CoM vectors, one could use, for example, topological segmentation of the 2D CoM vector field (Bujack et al., 2022). However, it is not possible to

determine if a boundary in the CoM vector field represents an intra-granular fracture, grain or subgrain boundary, even if the underlying mineral is known from XFM (e.g., Figs. 7b, 9e). If registered transmitted-light micrographs are available, as in our study, this problem can be solved qualitatively in all cases. However, our analysis of the recorded NR (Section 3.3) demonstrates that a pathway towards full orientation analysis from XBDM exists: the look-up table method implemented for the Maia detector system by Kirkwood et al. (2018).

4.3. Optimising XBDM scanning protocols

To produce the full energy-dispersive dataset for the XBDM ROI analysed in this work (Fig. 3a), 24 energies were scanned for an area of 7.2 mm^2 at a resolution of 2 μm per pixel, requiring a total scan time of 12 h and 24 min. For the EBSD test, ca. 1% of the total XBDM ROI were mapped over 1 h and 18 min at 1 μm per pixel resolution without recording EDS concurrently. In terms of scan rate (pixels scanned per second), XBDM was recorded at ca. 1000 Hz and EBSD at 13 Hz. Accounting for the difference in spatial resolution, XBDM acquisition was thus close to 20 times faster than that of the used EBSD system while also delivering high-sensitivity XFM maps mapping trace elements with concentrations <10 ppm (Fig. 7). If one would add EDS-/WDS-mapping
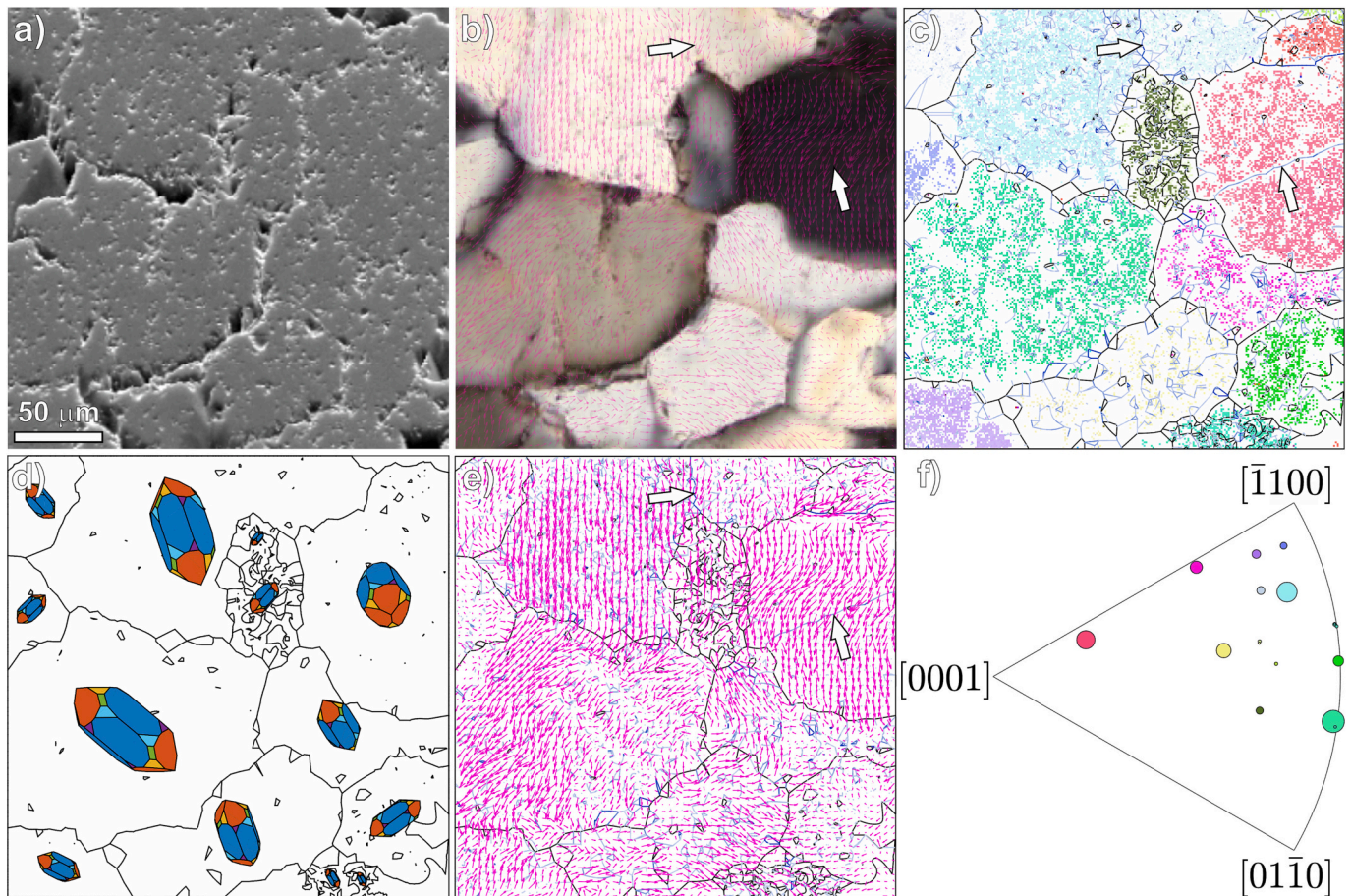

Fig. 9. Qualitative comparison between EBSD and CoM results. a) Secondary-electron micrograph of the quartz-ribbon region examined with EBSD. Significant surface damage due to the auto-polisher is visible. b) XPL micrograph of the region. White arrows mark exemplary subgrain boundaries identified with EBSD. CoM position vectors are superposed in transparent magenta colours at ca. 25% data density. c) Plot of regions successfully indexed by EBSD, coloured according to orientation. The colour scale is given in the inverse-pole figure underneath the plot. The boundaries of grains (black lines) and subgrains (blue lines, transparency scales inversely with misorientation) were computed via MTEX (Bachmann et al., 2010) with the approach of Bachmann et al. (2011), using the lower and upper misorientation bounds of 1° and 15°, respectively. d) Alternative visualisation of mean-grain orientation determined via EBSD through models of idiomorphic quartz crystals (for large grains only). The associated MTEX function employs the approach of Enderlein (1997). e) Grain and subgrain boundaries from EBSD superposed with CoM vectors. f) Inverse-pole figure for mean-grain orientation relative to the image-normal direction. The coloured circles represent the mean orientation of grains, and their size scales with grain size (see panel c). (For interpretation of the references to colour in this figure legend, the reader is referred to the web version of this article.)

to the time budget of conventional electron-beam analysis, the time advantage of XFM/XBDM would easily exceed a factor 100.

However, the question arises: are 24 energy increments needed to conduct the XBDM analysis presented here? Reducing the number of energy scans would speed up XFM/XBDM acquisition. To answer this question, we produced and analysed eight partial datasets, processing only the first energy scan at 5205 eV, followed by the first three, the first six, et cetera (Fig. 10). The proportion of mapped pixels that record Bragg reflections shows a highly non-linear response when plotted against the number of used energies (Fig. 10a). For a single map, only 53% of all pixels record diffractions. However, the curve saturates at 12 energies (i.e., 50% of the total dataset) with >99% of all pixels recording diffractions. Plotting the proportion of pixels with NR $\geq$ 4 (the number required for deriving the crystal orientation with the look-up table method (Kirkwood et al., 2018)) for the four main minerals as function of the number of energies yields a qualitatively similar response with important mineral-specific differences. For the feldspars and mica, the curves saturate at ca. 10 energies with >98% of all pixels recording NR $\geq$ 4. In contrast, only 60% of pixels within quartz achieve NR $\geq$ 4 at this energy count. The quartz curve flattens out to saturation at the used 24 energies. Therefore, if low-symmetry minerals are targeted by XFM/XBDM analysis, recording 10 to 12 energies should be enough to obtain excellent XBDM coverage. If highly symmetric minerals such as quartz are investigated, at least 20 energies should be scanned for measuring >90% solvable XBDM pixels.

4.4. Challenges of XFM/XBDM

XFM/XBDM is a volumetric scanning method because, in practice, fluorescence (XFM) and elastically diffracted (XBDM) photons are recovered from the sample spot up to a mineral-, energy-, and element-specific depth (Supplementary Fig. 3, see also Schrank et al. (2021)) referred to as X-ray attenuation length (Henke et al., 1993; Jackson and Hawkes, 1981). At the attenuation length, the X-ray penetrating the sample has dropped to 1/e (~37%) of its incident intensity due to a combination of elastic scattering, inelastic scattering, and the photoelectric effect (Jackson and Hawkes, 1981). X-rays leaving the sample from depth continue to experience attenuation. The attenuation length is the inverse of the linear attenuation coefficient, which in turn is the product of the number of atoms per unit volume and the total X-ray atomic attenuation cross-section of a material (i.e., the sum of the atomic attenuation cross-sections for elastic and inelastic scattering as well as the photoelectric effect) (Jackson and Hawkes, 1981). All contributions to the total attenuation cross-section depend on atomic number. Therefore, the attenuation length is material-specific (Supplementary Fig. 3). The energy dependence of attenuation length arises because the atomic attenuation cross-sections for inelastic scattering and the photoelectric effect are energy-dependent (Jackson and Hawkes, 1981).

Finally, the specific depth (i.e., attenuation length), to which fluorescence photons can be measured with XFM, also depends on the target element itself (Supplementary Fig. 3 shows examples for Ca, K, Si, and Ti) because the fluorescence energy of the emitted photons is controlled by the element-specific orbital structure (Jenkins and De Vries, 1969). As a result, different elements and elastic diffractions are measured to differing depths in different minerals. This volumetric measurement capacity can be an advantage, for example, when targeting trace elements embedded in micrometre-sized minerals dispersed within larger grains (e.g., Figs. 7, 10; see Schrank et al. (2021) for an application). However, it can also render data interpretation and analysis more challenging, namely when investigating materials with grain sizes well below the sample thickness. In this instance, a single pixel might contain information from several stacked grains (overprinting). In XBDM analysis, such a scenario would lead to multi-lattice diffractions, which would render indexing and orientation determination difficult. Methods for the indexing of multi-lattice diffractions require the sampling of >10 elastic reflections with very accurate measurements of their directions (Gildea et al., 2014) and are thus not well suited to the XBDM data acquired with the Maia detector. The simplest way out of the dilemma is to restrict XBDM analysis to regions where the mean grain size is much larger than sample thickness, as is the case in most of our test sample. Second, sample thickness can be reduced by the manufacture of ultra-thin sections. However, the trade-off is that a thickness reduction also reduces the amount of material within the sample-spot volume, which will result in a weaker XFM/XBDM signal. Finally, one can move the scanned energy window to lower values to restrict XBDM measurements to, say, the upper 10 μm of the sample. In our experiment, elastic diffractions were measured to depths >20 μm (Supplementary Fig. 3). Regardless of sample grain size, the challenge of multi-lattice diffractions from overlapping grains always arises near grain boundaries that are not normal to the sample surface. Hence, a refinement of any indexing approach will be required that treats such grain-boundary pixels separately, such as the one implemented by Kirkwood et al. (2018). Moreover, rigorous quantitative methods for mapping and analysing grain boundaries have been developed by the EBSD community (e.g., Bachmann et al., 2011; McMahon et al., 2013) and can be adopted to XBDM analysis.

5. Conclusions

We demonstrated high speed and high sensitivity of coeval XFM/XBDM measurements that permit the quantitative, coeval mapping of a wealth of structural and chemical information, spanning length scales from that of the crystal lattice (10^{-10} m) to that of the hand specimen (10^{-2} m) in a single measurement. Applying this method to typical deformed crustal rocks, we obtain collocated millimetre-scale elemental-concentration and simplified grain-orientation maps with
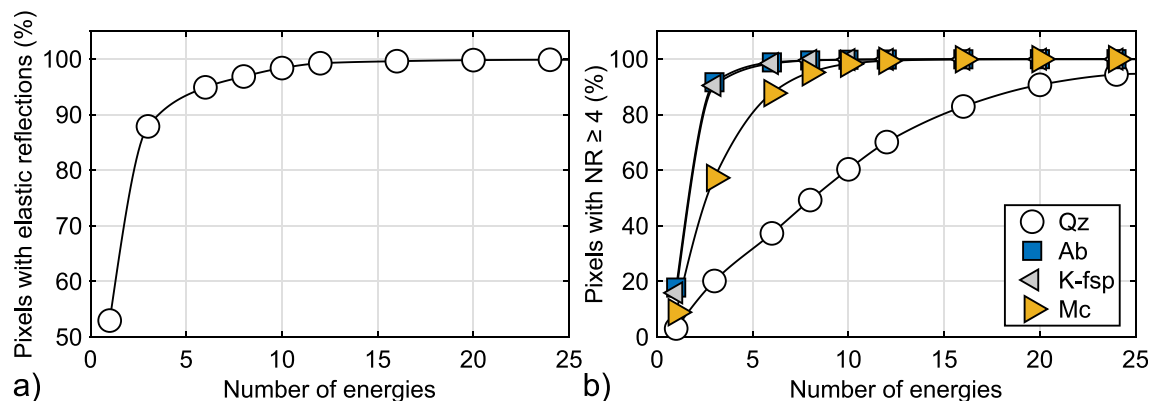

Fig. 10. a) Proportion of pixels in the XBDM ROI that produced elastic reflections as function of the number of energy scans used for processing. b) Mineral-specific proportion of pixels with NR $\geq$ 4 as function of the number of energy scans. The black solid lines serve as visual guide for the data trend only.

very high speed at micrometre resolution and >99% coverage for orientation solutions, showing how crystal-plastic deformation mobilises Ti during deformation, precipitating along newly formed subgrains, grain boundaries, and cracks in a mylonite (Fig. 7).

The main outcomes of our study are:

(1) XFM/XBDM delivers perfectly registered maps of trace-element concentrations and grain orientation (Figs. 4, 7–9) rapidly over large areas without the need for complicated sample preparation.

(2) The simplified approach to visualising crystal structure via the centre of mass of the measured Bragg diffractions permits an accurate qualitative identification of inter- and intragranular interfaces such as grain and subgrain boundaries as well as fractures (Figs. 7, 9).

(3) Mapping the scattering intensity (Fig. 4) and the number of Bragg reflections per pixel (NR, Figs. 5, 8) provide a simple and fast method for imaging phase and grain boundaries and can be used to guide further in-depth investigations with minimal time cost.

(4) XBDM analysis yields >99% success rate for rock sections with standard polishing and thus requires less difficult sample preparation than EBSD.

(5) For the rock-forming minerals quartz, feldspar, and mica, the presented XBDM scanning strategy delivers >94% of mapped pixels with enough elastic diffractions to enable full orientation analysis via the look-up table method (Kirkwood et al., 2018). Implementation of this method is underway.

(6) XFM/XBDM mapping is about two orders of magnitude faster and more sensitive for trace-element mapping than combined chemical-structural mapping with conventional electron-beam instruments. A measurement like ours would take over 1000 h on a conventional electron-beam instrument.

XFM/XBDM mapping will thus enable researchers to conduct rigorous non-destructive quantitative microchemical and microstructural studies of complex geological specimens at the millimetre to centimetre scale. Selected scientific applications where this method provides significant advantages include:

1) Studies that examine if trace elements with low concentrations (<100 ppm) are mobilised by crystal-plastic deformation (e.g., Bestmann et al. (2021); MacDonald et al. (2013); Figs. 6–8).

2) Surveys where it is important to map large areas at high resolution (Fig. 6), for example, to detect small, rare particles (the proverbial needle in the haystack, Howard et al. (2020); Lintern et al. (2013)) or when a statistically representative number of features needs to be observed in heterogeneous samples (e.g., Barnes et al., 2017; Schrank et al., 2021).

3) Investigations that probe for narrow elemental pathways such as grain and subgrain boundaries or microfractures (Figs. 7, 8, e.g., Akker et al. (2023); Tacchetto et al. (2021)). In this instance, it is necessary that the registration error between microchemical and -structural maps is minimized.

4) XFM/XBDM analysis enables spatially resolved full mass-balance analyses across deformation structures (e.g., Schrank et al., 2021).

In the light of these findings, we anticipate that XFM/XBDM will inspire fundamental discoveries in our understanding of the coupling of rock deformation, fluid flow, and chemical reactions in the near future (Jones et al., 2022; Schrank et al., 2021).

Author contributions

Christoph E. Schrank: conceptualization, funding acquisition, formal analysis, visualisation, writing – original draft, review & editing. Michael W. M. Jones: conceptualization, funding acquisition, formal analysis, visualisation, writing – review & editing. Daryl L. Howard: conceptualization, experimentation, formal analysis, writing – review & editing. Alfons Berger and Marco Herwegh: conceptualization, field work and sample collection, writing – review & editing.

CRediT authorship contribution statement

C.E. Schrank: Writing – review & editing, Writing – original draft, Visualization, Validation, Methodology, Investigation, Funding acquisition, Formal analysis, Data curation, Conceptualization. **M.W.M. Jones:** Writing – review & editing, Visualization, Validation, Methodology, Investigation, Funding acquisition, Formal analysis, Data curation, Conceptualization. **D.L. Howard:** Writing – review & editing, Methodology, Investigation, Formal analysis, Conceptualization. **A. Berger:** Writing – review & editing, Resources, Investigation, Conceptualization. **M. Herwegh:** Writing – review & editing, Resources, Investigation, Conceptualization.

Declaration of Competing Interest

The authors have no competing interests to declare in regards to the submitted manuscript.

Data availability

Data will be made available on request.

Acknowledgements

Appendix A. Supplementary data

Supplementary data to this article can be found online at https://doi.org/10.1016/j.chemgeo.2023.121886.

References

Acevedo Zamora, M.A., Kamber, B.S., 2023. Petrographic Microscopy with Ray Tracing and Segmentation from Multi-Angle Polarisation Whole-Slide Images. Minerals 13, 156. https://doi.org/10.3390/min13020156.

Akker, I.V., Berger, A., Schrank, C.E., Jones, M.W.M., Kewish, C.M., Klaver, J., Herwegh, M., 2021. The evolution of slate microfabrics during progressive accretion of foreland basin sediments. J. Struct. Geol. 150, 104404.

Akker, I.V., Schrank, C., Herwegh, M., Berger, A., Jones, M., Kewish, C.M., 2023. The geometry, spatial distribution and texture of slate-hosted calcite veins in the helvetic flysch units—insights in structural and fluid processes within a paleo-accretionary complex. Geochem. Geophys. Geosyst. 24 e2023GC010873.

Bachmann, F., Hielscher, R., Schaeben, H., 2010. Texture analysis with MTEX – free and open source software toolbox. Solid State Phenom. 160, 63–68.

Bachmann, F., Hielscher, R., Schaeben, H., 2011. Grain detection from 2d and 3d EBSD data—specification of the MTEX algorithm. Ultramicroscopy 111, 1720–1733.

Balluffi, R.W., Sass, S.L., Schober, T., 1972. Grain boundary dislocation networks as electron diffraction gratings. Philos. Mag. J. Theoret. Exp. Appl. Phys. 26, 585–592.

Bambauer, H.U., Herwegh, M., Kroll, H., 2009. Quartz as indicator mineral in the Central Swiss Alps: the quartz recrystallization isograd in the rock series of the northern Aar massif. Swiss J. Geosci. 102, 345–351.

Barnes, S.J., Mungall, J.E., Le Vaillant, M., Godel, B., Lesher, C.M., Holwell, D., Lightfoot, P.C., Krivolutskaya, N., Wei, B., 2017. Sulfide-silicate textures in magmatic Ni-Cu-PGE sulfide ore deposits: Disseminated and net-textured ores. Am. Mineral. 102, 473–506.

Barnes, S.J., Paterson, D., Ubide, T., Schoneveld, L.E., Ryan, C., Le Vaillant, M., 2020. Imaging trace-element zoning in pyroxenes using synchrotron XRF mapping with the Maia detector array: benefit of low-incident energy. Am. Mineral. 105, 136–140.

Berger, A., Wehrens, P., Lanari, P., Zwingmann, H., Herwegh, M., 2017. Microstructures, mineral chemistry and geochronology of white micas along a retrograde evolution: an example from the Aar massif (Central Alps, Switzerland). Tectonophysics 721, 179–195.

Bestmann, M., Pennacchioni, G., 2015. Ti distribution in quartz across a heterogeneous shear zone within a granodiorite: the effect of deformation mechanism and strain on Ti resetting. Lithos 227, 37–56.

Bestmann, M., Pennacchioni, G., Grasemann, B., Huet, B., Jones, M.W.M., Kewish, C.M., 2021. Influence of deformation and fluids on ti exchange in natural quartz. J. Geophys. Res. Solid Earth 126 e2021JB022548.

Bujack, R., Bresciani, E., Waters, J., Schroeder, W., 2022. Topological Segmentation of 2D Vector Fields.

Catlos, E.J., Lovera, O.M., Kelly, E.D., Ashley, K.T., Harrison, T.M., Etzel, T., 2018. Modeling high-resolution pressure-temperature paths across the Himalayan main central thrust (central Nepal): implications for the dynamics of collision. Tectonics 37, 2363–2388.

Ceccato, A., Goncalves, P., Menegon, L., 2022. On the petrology and microstructures of small-scale ductile shear zones in granitoid rocks: an overview. J. Struct. Geol. 161, 104667.

Challandes, N., Marquer, D., Villa, I.M., 2008. P-T-t modelling, fluid circulation, and 39Ar-40Ar and Rb-Sr mica ages in the Aar Massif shear zones (Swiss Alps). Swiss J. Geosci. 101, 269–288.

Choukroune, P., Gapais, D., 1983. Strain pattern in the Aar Granite (Central Alps): orthogneiss developed by bulk inhomogeneous flattening. In: Cobbold, P.R., Schwerdtner, W.M., Treagus, S.H. (Eds.), Strain Patterns in Rocks. Pergamon, pp. 411–418.

Ebert, A., Herwegh, M., Evans, B., Pfiffner, A., Austin, N., Vennemann, T., 2007. Microfabrics in carbonate mylonites along a large-scale shear zone (Helvetic Alps). Tectonophysics 444, 1–26.

Egglseder, M.S., Cruden, A.R., Tomkins, A.G., Wilson, S., Dalstra, H.J., Rielli, A., Li, C., Baumgartner, J., Faivre, D., 2019. Tiny particles building huge ore deposits – particle-based crystallisation in banded iron formation-hosted iron ore deposits (Hamersley Province, Australia). Ore Geol. Rev. 104, 160–174.

Enderlein, J., 1997. A package for displaying crystal morphology. Math. J. 7, 72–78.

Gildea, R.J., Waterman, D.G., Parkhurst, J.M., Axford, D., Sutton, G., Stuart, D.I., Sauter, N.K., Evans, G., Winter, G., 2014. New methods for indexing multi-lattice diffraction data. Acta Crystallogr. Sect. D 70, 2652–2666.

Gilgannon, J., Poulet, T., Berger, A., Barnhoorn, A., Herwegh, M., 2020. Dynamic recrystallization can produce porosity in shear zones. Geophys. Res. Lett. 47 e2019GL086172.

Goncalves, P., Oliot, E., Marquer, D., Connolly, J.A.D., 2012. Role of chemical processes on shear zone formation: an example from the Grimsel metagranodiorite (Aar massif, Central Alps). J. Metam. Geol. 30, 703–722.

Gottlieb, P., Wilkie, G., Sutherland, D., Ho-Tun, E., Suthers, S., Perera, K., Jenkins, B., Spencer, S., Butcher, A., Rayner, J., 2000. Using quantitative electron microscopy for process mineralogy applications. JOM 52, 24–25.

Gueriau, P., Réguer, S., Leclercq, N., Cupello, C., Brito, P.M., Jauvion, C., Morel, S., Charbonnier, S., Thiaudière, D., Mocuta, C., 2020. Visualizing mineralization processes and fossil anatomy using synchronous synchrotron X-ray fluorescence and X-ray diffraction mapping. J. R. Soc. Interface 17, 20200216.

Hamilton, J.G., Reid, J.W., Feng, R., Peak, D., 2018. Evaluating synchrotron-based scanning laue microdiffraction for mineralogy mapping in heterogeneous samples. ACS Earth Space Chem. 2, 1161–1167.

Henke, B.L., Gullikson, E.M., Davis, J.C., 1993. X-ray interactions: photoabsorption, scattering, transmission, and reflection at E = 50-30,000 eV, Z = 1-92. At. Data Nucl. Data Tables 54, 181–342.

Herwegh, M., 2000. A new technique to automatically quantify microstructures of fine grained carbonate mylonites: two-step etching combined with SEM imaging and image analysis. J. Struct. Geol. 22, 391–400.

Herwegh, M., Kunze, K., 2002. The influence of nano-scale second-phase particles on deformation of fine grained calcite mylonites. J. Struct. Geol. 24, 1463–1478.

Herwegh, M., Berger, A., Ebert, A., Brodhag, S., 2008. Discrimination of annealed and dynamic fabrics: consequences for strain localization and deformation episodes of large-scale shear zones. Earth Planet. Sci. Lett. 276, 52–61.

Herwegh, M., Berger, A., Baumberger, R., Wehrens, P., Kissling, E., 2017. Large-scale crustal-block-extrusion during late alpine collision. Sci. Rep. 7, 413.

Herwegh, M., Berger, A., Glotzbach, C., Wangenheim, C., Mock, S., Wehrens, P., Baumberger, R., Egli, D., Kissling, E., 2020. Late stages of continent-continent collision: timing, kinematic evolution, and exhumation of the Northern rim (Aar Massif) of the Alps. Earth Sci. Rev. 200, 102959.

Hirth, J.P., Balluffi, R.W., 1973. On grain boundary dislocations and ledges. Acta Metall. 21, 929–942.

Hirth, G., Teyssier, C., Dunlap, J., 2001. An evaluation of quartzite flow laws based on comparisons between experimentally and naturally deformed rocks. Int. J. Earth Sci. 90, 77–87.

Howard, D.L., de Jonge, M.D., Afshar, N., Ryan, C.G., Kirkham, R., Reinhardt, J., Kewish, C.M., McKinlay, J., Walsh, A., Divitcos, J., Basten, N., Adamson, L., Fiala, T., Sammut, L., Paterson, D.J., 2020. The XFM beamline at the Australian Synchrotron. J. Synchrotron Radiat. 27, 1447–1458.

Howe, N., 2023. 2D Vector Field Visualization. MATLAB Central File Exchange.

Hrstka, T., Gottlieb, P., Skala, R., Breiter, K., Motl, D., 2018. Automated mineralogy and petrology - applications of TESCAN Integrated Mineral Analyzer (TIMA). J. Geosci. 63, 47–63.

Jackson, D.F., Hawkes, D.J., 1981. X-ray attenuation coefficients of elements and mixtures. Phys. Rep. 70, 169–233.

Jenkins, R., De Vries, J.L., 1969. Physics of X-RAYS. In: Jenkins, R., De Vries, J.L. (Eds.), Practical X-Ray Spectrometry. Springer US, New York, NY, pp. 1–25.

Jones, M.W.M., van Riessen, G.A., Phillips, N.W., Schrank, C.E., Hinsley, G.N., Afshar, N., Reinhardt, J., de Jonge, M.D., Kewish, C.M., 2022. High-speed free-run ptychography at the Australian Synchrotron. J. Synchrotron Radiat. 29, 480–487.

Kanaori, Y., Yairi, K., Ishida, T., 1991. Grain boundary microcracking of granitic rocks from the northeastern region of the Atotsugawa fault, central Japan: SEM backscattered electron images. Eng. Geol. 30, 221–235.

Kirkwood, H.J., de Jonge, M.D., Muransky, O., Hofmann, F., Howard, D.L., Ryan, C.G., van Riessen, G.A., Rowles, M.R., Paradowska, A.M., Abbey, B., 2018. Simultaneous X-ray diffraction, crystallography, and fluorescence mapping using the Maia detector. Acta Mater. 144, 1–10.

Kruhl, J.H., Wirth, R., Morales, L.F.G., 2013. Quartz grain boundaries as fluid pathways in metamorphic rocks. J. Geophys. Res. Solid Earth 118, 1957–1967.

Lapkin, D., Kirsch, C., Hiller, J., Andrienko, D., Assalauova, D., Braun, K., Carnis, J., Kim, Y.Y., Mandal, M., Maier, A., Meixner, A.J., Mukharamova, N., Scheele, M., Schreiber, F., Sprung, M., Wahl, J., Westendorf, S., Zaluzhnyy, I.A., Vartanyants, I. A., 2022. Spatially resolved fluorescence of caesium lead halide perovskite supercrystals reveals quasi-atomic behavior of nanocrystals. Nat. Commun. 13, 892.

Law, R.D., 2014. Deformation thermometry based on quartz c-axis fabrics and recrystallization microstructures: a review. J. Struct. Geol. 66, 129–161.

Lintern, M., Anand, R., Ryan, C., Paterson, D., 2013. Natural gold particles in Eucalyptus leaves and their relevance to exploration for buried gold deposits. Nat. Commun. 4, 2614.

Liu, Y., Tice, M.M., Schmidt, M.E., Treiman, A.H., Kizovski, T.V., Hurowitz, J.A., Allwood, A.C., Henneke, J., Pedersen, D.A.K., VanBommel, S.J., Jones, M.W.M., Knight, A.L., Orenstein, B.J., Clark, B.C., Elam, W.T., Heirwegh, C.M., Barber, T., Beegle, L.W., Benzerara, K., Bernard, S., Beyssac, O., Bosak, T., Brown, A.J., Cardarelli, E.L., Catling, D.C., Christian, J.R., Cloutis, E.A., Cohen, B.A., Davidoff, S., Fairén, A.G., Farley, K.A., Flannery, D.T., Galvin, A., Grotzinger, J.P., Gupta, S., Hall, J., Herd, C.D.K., Hickman-Lewis, K., Hodyss, R.P., Horgan, B.H.N., Johnson, J. R., Jørgensen, J.L., Kah, L.C., Maki, J.N., Mandon, L., Mangold, N., McCubbin, F.M., McLennan, S.M., Moore, K., Nachon, M., Nemere, P., Nothdurft, L.D., Núñez, J.I., O'Neil, L., Quantin-Nataf, C.M., Sautter, V., Shuster, D.L., Siebach, K.L., Simon, J.I., Sinclair, K.P., Stack, K.M., Steele, A., Tarnas, J.D., Tosca, N.J., Uckert, K., Udry, A., Wade, L.A., Weiss, B.P., Wiens, R.C., Williford, K.H., Zorzano, M.-P., 2022. An olivine cumulate outcrop on the floor of Jezero crater, Mars. Science 377, 1513–1519.

MacDonald, J.M., Wheeler, J., Harley, S.L., Mariani, E., Goodenough, K.M., Crowley, Q., Tatham, D., 2013. Lattice distortion in a zircon population and its effects on trace element mobility and U–Th–Pb isotope systematics: examples from the Lewisian Gneiss Complex, northwest Scotland. Contrib. Mineral. Petrol. 166, 21–41.

McMahon, C., Soe, B., Loeb, A., Vemulkar, A., Ferry, M., Bassman, L., 2013. Boundary identification in EBSD data with a generalisation of fast multiscale clustering. Ultramicroscopy 133, 16–25.

Orenstein, B.J., Flannery, D.T., Casey, L.W., Elam, W.T., Heirwegh, C.M., Jones, M.W.M., 2023. A statistical approach to removing diffraction from X-ray fluorescence spectra. Spectrochim. Acta B At. Spectrosc. 200, 106603.

Passchier, C.W., Trouw, R.A.J., 2005. Microtectonics. Springer.

Pecharsky, V.K., Zavalij, P.Y., 2009. Fundamentals of Powder Diffraction and Structural Characterization of Materials, Second ed. Springer Science+Business Media, New York.

Pfeiffer, F., 2018. X-ray ptychography. Nat. Phys. 12, 9–17.

Raimbourg, H., Toyoshima, T., Harima, Y., Kimura, G., 2008. Grain-size reduction mechanisms and rheological consequences in high-temperature gabbro mylonites of Hidaka, Japan. Earth Planet. Sci. Lett. 267, 637–653.

Reed, S.J.B., 2005. Electron Microprobe Analysis and Scanning Electron Microscopy in Geology, 2 ed. Cambridge University Press, Cambridge.

Ryan, C.G., Jamieson, D.N., 1993. Dynamic analysis: on-line quantitative PIXE microanalysis and its use in overlap-resolved elemental mapping. Nucl. Instrum. Methods Phys. Res., Sect. B 77, 203–214.

Ryan, C.G., Etschmann, B.E., Vogt, S., Maser, J., Harland, C.L., van Achterbergh, E., Legnini, D., 2005. Nuclear microprobe - synchrotron synergy: towards integrated quantitative real-time elemental imaging using PIXE and SXRF. Nucl. Inst. Methods Phys. Res. B 231, 183–188.

Ryan, C.G., Kirkham, R., Siddons, D.P., Dunn, P.A., Laird, J.S., Kuczewski, A., Moorhead, G., De Geronimo, G., Davey, P., Jensen, M., Paterson, D.J., de Jonge, M. D., Howard, D.L., Hough, R.M., 2010. The Maia 384 detector array in a nuclear microprobe: a platform for high definition PIXE elemental imaging. Nucl. Instrum. Methods Phys. Res., Sect. B 268, 1899–1902.

Ryan, C., Kirkham, R., de Jonge, M., Siddons, D., Ent, A., Pagés, A., Bösenberg, U., Kuczewski, A., Dunn, P., Jensen, M., Liu, W., Harris, H., Moorhead, G., Paterson, D., Howard, D., Afshar, N., Garrevoet, J., Spiers, K., Falkenberg, G., Pearce, M., 2018. The maia detector and event mode. Synchrotron Radiat. News 31, 21–27.

Schaltegger, U., Corfu, F., 1992. The age and source of late Hercynian magmatism in the central Alps: evidence from precise U–Pb ages and initial Hf isotopes. Contrib. Mineral. Petrol. 111, 329–344.

Schrank, C.E., Jones, M.W.M., Kewish, C.M., van Riessen, G.A., Elphick, K.E., Nothdurft, L.D., Webb, G.E., Paterson, D.J., Regenauer-Lieb, K., 2021. Micro-scale dissolution seams mobilise carbon in deep sea limestones. Commun. Earth Environ. 2, 174.

Schwartz, A.J., Kumar, M., Adams, B.L., Field, D.P., 2009. Electron Backscatter Diffraction in Materials Science, 2nd ed. Springer New York, NY.

Siddons, D.P., Kirkham, R., Ryan, C.G., De Geronimo, G., Dragone, A., Kuczewski, A.J., Li, Z.Y., Carini, G.A., Pineli, D., Beuttenmuller, R., Elliot, D., Pfeffer, M., Tyson, T.A., Moorhead, G.F., Dunn, P.A., 2014. Maia X-ray microprobe detector array system. J. Phys. Conf. Ser. 499, 012001.

Stipp, M., Stünitz, H., Heilbronner, R., Schmid, S.M., 2002. The eastern Tonale fault zone: a 'natural laboratory' for crystal plastic deformation of quartz over a temperature range from 250 to 700 °C. J. Struct. Geol. 24, 1861–1884.

Stromberg, J.M., Van Loon, L.L., Gordon, R., Woll, A., Feng, R., Schumann, D., Banerjee, N.R., 2019. Applications of synchrotron X-ray techniques to orogenic gold studies; examples from the Timmins gold camp. Ore Geol. Rev. 104, 589–602.

Tacchetto, T., Reddy, S.M., Saxey, D.W., Fougerouse, D., Rickard, W.D.A., Clark, C., 2021. Disorientation control on trace element segregation in fluid-affected low-angle boundaries in olivine. Contrib. Mineral. Petrol. 176, 59.

Tannock, L., Herwegh, M., Berger, A., Liu, J., Lanari, P., Regenauer-Lieb, K., 2020. Microstructural analyses of a giant quartz reef in South China reveal episodic brittle-ductile fluid transfer. J. Struct. Geol. 130, 103911.

Tice, M.M., Hurowitz, J.A., Allwood, A.C., Jones, M.W.M., Orenstein, B.J., Davidoff, S., Wright, A.P., Pedersen, D.A.K., Henneke, J., Tosca, N.J., Moore, K.R., Clark, B.C., McLennan, S.M., Flannery, D.T., Steele, A., Brown, A.J., Zorzano, M.-P., Hickman-Lewis, K., Liu, Y., VanBommel, S.J., Schmidt, M.E., Kizovski, T.V., Treiman, A.H., O'Neil, L., Fairén, A.G., Shuster, D.L., Gupta, S., The, P.T., 2022. Alteration history of Séítah formation rocks inferred by PIXL x-ray fluorescence, x-ray diffraction, and multispectral imaging on Mars. Sci. Adv. 8, eabp9084.

van Riessen, A., Rickard, W.D.A., Williams, R.P., van Riessen, G.A., 2017. Methods for geopolymer formulation development and microstructural analysis. J. Ceramic Sci. Technol. 8, 421–432.

von der Heyden, B.P., 2020. Shedding light on ore deposits: a review of synchrotron X-ray radiation use in ore geology research. Ore Geol. Rev. 117, 103328.

Wark, D.A., Watson, E.B., 2006. TitaniQ: a titanium-in-quartz geothermometer. Contrib. Mineral. Petrol. 152, 743–754.

Wehrens, P., Berger, A., Peters, M., Spillmann, T., Herwegh, M., 2016. Deformation at the frictional-viscous transition: evidence for cycles of fluid-assisted embrittlement and ductile deformation in the granitoid crust. Tectonophysics 693, 66–84.

Wehrens, P., Baumberger, R., Berger, A., Herwegh, M., 2017. How is strain localized in a meta-granitoid, mid-crustal basement section? Spatial distribution of deformation in the central Aar massif (Switzerland). J. Struct. Geol. 94, 47–67.

Wright, S.I., Nowell, M.M., Field, D.P., 2011. A review of strain analysis using electron backscatter diffraction. Microsc. Microanal. 17, 316–329.

Zhang, Y., Gu, X., Rusk, B., Mao, W., Wang, J., Zheng, S., 2022. In situ trace elements in quartz and K-feldspar from felsic igneous rocks: a titanium-in-K-feldspar geothermometer for natural magmatic systems. J. Petrol. 63, egac113.